Xiaowei Cheng, Xiaodong Ji, Richard S. Henry, Mengchao Xu. Coupled axial tension-flexure behavior of slender reinforced concrete Walls. Engineering Structures, 2019, 188: 261-276.

Coupled Axial Tension-Flexure Behavior of Slender Reinforced Concrete Walls

Xiaowei Cheng[a], Xiaodong Ji[b], Richard S. Henry[c], Mengchao Xu[d]

[a]*National Engineering Laboratory for Green and Safe Construction Technology in Urban Rail Transit, Tsinghua University, Beijing 100084, China*

[b]*Associate professor, Key Laboratory of Civil Engineering Safety and Durability of China Education Ministry, Department of Civil Engineering, Tsinghua University, Beijing 100084, China*

[c]*Senior Lecturer, Department of Civil and Environmental Engineering, The University of Auckland, Auckland 1010, New Zealand*

[d]*Graduate student, Department of Civil Engineering, Tsinghua University, Beijing100084, China*

Abstract: Reinforced concrete (RC) walls in high-rise buildings, in particular wall piers that form part of a coupled or core wall system, may experience coupled axial tension-flexure loading when subjected to lateral demands. The seismic behavior of RC walls with various axial tensile forces was investigated by quasi-static tests on four RC slender walls subjected to the combined tension and flexure loading. The failure modes, strength and deformation capacity, effective flexural stiffness, and design equations are presented. The failure modes included flexural-sliding failure and flexural failure. The effective flexural stiffness and lateral strength of the walls significantly decreased as the axial tensile forces were increased. The ACI 318-14 and ASCE/SEI 41-13 code provisions overestimated the effective flexural stiffness of RC walls subjected to axial

Please cite this article as: Xiaowei Cheng, Xiaodong Ji, Richard S. Henry, Mengchao Xu. Coupled axial tension-flexure behavior of slender reinforced concrete Walls. Engineering Structures, 2019, 188: 261-276. doi: 10.1016/j.engstruct.2019.03.026

tension. Although equations proposed by Paulay & Priestley and Adebar et al. consider the influence of axial forces, they were not able to accurately predict the effective flexural stiffness of the RC wall specimens subjected to tensile forces. Both sectional analysis using XTRACT and JGJ 3-2010 (China) code equations provided accurate estimation of the flexural yield strength of walls. Finally, both a refined model and simplified equation were proposed to estimate the axial elongation for RC slender walls subjected to axial tensile force and cyclic lateral loading.

Keywords: Reinforced concrete walls; Coupled axial tension-flexure behavior; Effective flexural stiffness; Design equations; Strength; Axial elongation.

1. Introduction

Reinforced concrete (RC) walls are widely used as the major lateral load-resisting components in high-rise buildings. When subjected to strong ground motions, some structural walls, in particular wall piers that form part of a coupled or core wall system, may experience combined axial tension-flexure-shear load. For example, in a coupled wall system with a high coupling ratio the axial forces induced by coupling beam shears may result in the wall pier sustaining a net axial tensile force, combined with shear and bending actions induced by lateral loading, as illustrated in Fig. 1(a). Another example is a core wall under bi-directional ground motion, as shown in Fig. 1(b), where the peripheral wall is subjected to the tensile force caused by a large overturning moment from lateral loading in one direction, and the shear and bending actions induced by lateral loading in the perpendicular direction. Past earthquake reconnaissance (e.g., the 2010 Chile earthquake [1]), and experimental tests of coupled and core wall systems (e.g., [2-5]) identified such critical loading conditions for RC walls in high-rise buildings.

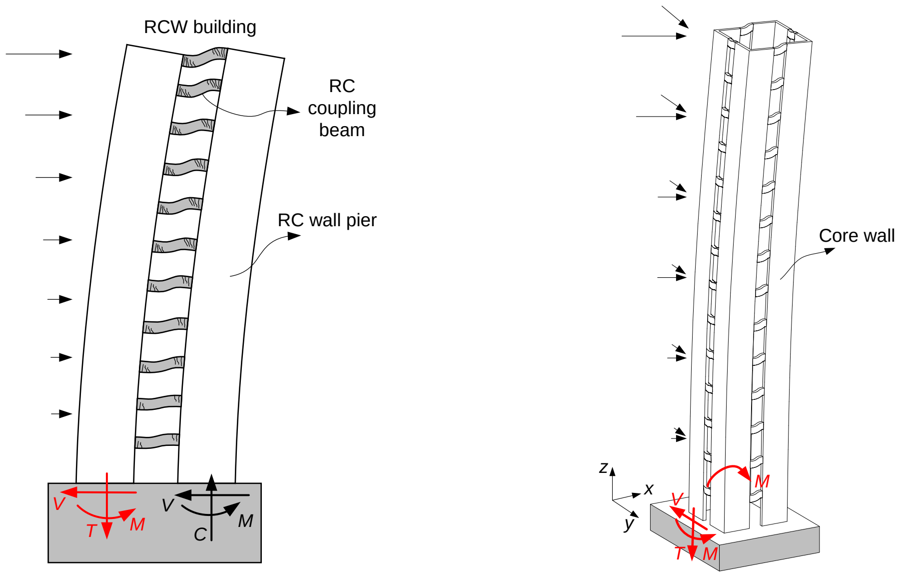

(a) Coupled wall (b) Core wall

Fig. 1. RC walls undergoing combined axial tension-flexure-shear actions.

Past research indicates that axial tension leads to decreased lateral stiffness and strength for RC members, which may result in force redistribution among structural components [2-5]. Therefore, special attention shall be given to RC walls that may be subjected to combined axial tension-flexure-shear during seismic design of high-rise buildings. However, fundamental experimental research on combined axial tension-flexure-shear behavior of RC walls remains limited.

Recently an increased attention has been given to the behavior RC walls under complicated loading conditions. Structural walls are generally classified by wall aspect ratio or shear-to-span ratio. The slender wall (also named as “high-aspect-ratio wall”) is usually defined for walls having aspect ratio greater than approximately 2.0. The squat wall (also named as “low-aspect-ratio wall”) is defined for walls having aspect ratio less than approximately 1.0. The walls between these aspect ratios are referred to as the moderate-aspect-ratio wall. Wang et al. [6] and Ren et al. [7] conducted a series of tests of moderate-aspect-ratio RC walls subjected to axial tension and cyclic lateral loading. Various failure modes were observed which were related to the magnitude of applied axial tension, steel reinforcement ratio, and shear-to-flexure strength ratio. Ji et al. [8] presented the coupled axial tension-shear behavior of low-aspect-ratio RC walls, of which the strength was governed by shear and sliding, rather than flexure. The test results indicated that the axial tensile force significantly affected the failure modes, shear stiffness and lateral strength of RC walls. Design formulae of shear stiffness and strength of RC walls under axial tension were estimated using the test data.

This paper presents the coupled axial tension-flexure behavior of high-aspect-ratio RC walls that are designed to be flexure controlled in accordance with capacity design principles. A series of tests were conducted on large RC wall specimens subjected to tensile forces and cyclic lateral loading. The first objective of this study is to determine how axial tensile forces influence failure modes, flexural strength and stiffness of RC slender walls. The second objective is to calibrate design formulas used to calculate the stiffness and strength of RC walls for combined flexure and axial tensile load (e.g., as specified in ACI 318-14 (U.S. code) [9] and JGJ 3-2010 (China code) [10]). As the axial elongation of RC walls would result in force redistribution, a new refined mechanics model and simplified equation are developed to trace the axial elongation of RC walls subjected to axial tension and cyclic lateral loading.

2. Experimental Program

2.1. Test walls

The test walls were designed to represent structural walls in the lower stories of a high-rise building. The length and thickness of the prototype wall were 4.5 m and 0.54 m, respectively. To accommodate the capacity of the loading facility, the wall specimens were fabricated to 1/3 scale of the prototype wall, with a length and thickness of 1.5 m and 0.18 m, respectively. The wall had a clear height equal to 2.7 m. A total of four wall specimens (labeled as HSW1 to HSW4) were designed and fabricated, each with identical geometry dimensions and reinforcement details as shown in Fig. 2. A top beam and foundation beam were fabricated together with the wall to allow for load application and anchorage of the specimen to reaction floor. The specimens were casted in the vertical position. The foundation beams were initially fabricated, followed by construction of the wall and top beam. The surface of hardened concrete of the foundation beam was cleaned before casting of the wall concrete. The foundation and top beams were capacity designed to ensure they remained elastic during testing.

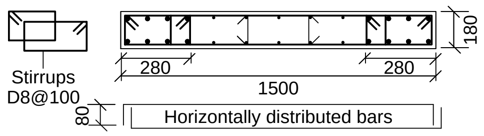

(a) Cross section

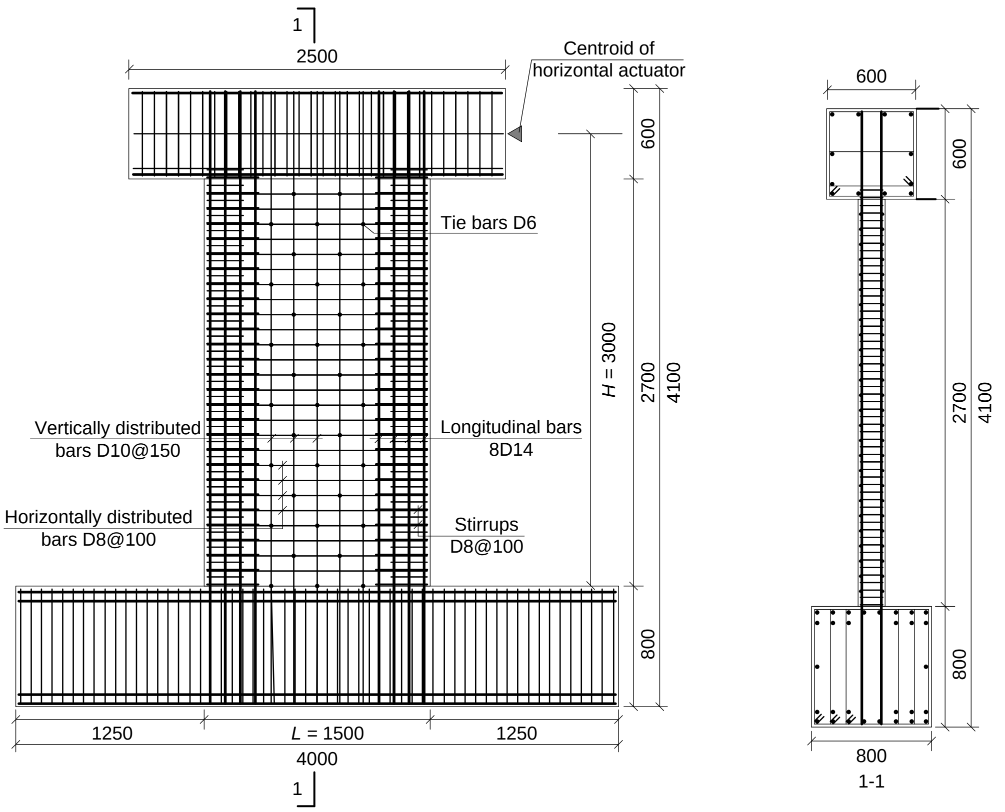

(b) Elevation view (c) Elevation view 1-1

Fig. 2. Geometry and reinforcement of specimens (units: mm).

Boundary elements, which extend for 280 mm from the wall edge, were designed for the walls. A total of eight D14 (diameter of 14 mm) steel reinforcing bars (hereinafter referred to as rebar) were used as longitudinal reinforcement for each boundary element, corresponding to a 2.3% reinforcement ratio (the ratio of gross cross-sectional area of longitudinal rebar to that of the boundary element). The vertically distributed reinforcement in the web comprised D10 steel rebar at a spacing of 150 mm, corresponding to a 0.58% reinforcement ratio. The horizontally distributed reinforcement comprised D8 steel rebar at a spacing of 100 mm, corresponding to a 0.56% reinforcement ratio. The boundary transverse reinforcement consisted of D8 steel rebar fabricated as rectangular hoops with a vertical spacing of 100 mm, corresponding to 1.5% volumetric transverse reinforcement ratio. The reinforcement ratios of the test specimens are within normal range used for the RC structural walls of high-rise buildings in China. The boundary elements and reinforcement of the specimens satisfied the requirement of seismic ductile walls specified in the Chinese Technical Specification for Concrete Structures for Tall Buildings (JGJ 3-2010) [10].

The strength grade of concrete used in the wall specimens was C35 (nominal cubic compressive strength $f_{cu,n}$ = 35 MPa). The aggregate size in the concrete ranged from 4.8 mm to 26.5 mm, with a mean value of approximately 16 mm. The measured compressive strength f_{cu} of the concrete using 150 mm cubes was 42.6, 27.9, 38.3 and 32.5 MPa for specimens HSW1 through HSW4. The value of f_{cu} was measured on the day of specimen testing, and it was taken as the average value for three cubes. The axial compressive strength of concrete f_c was taken as $0.76f_{cu}$ in accordance with the Chinese Code for Design of Concrete Structures GB 50010-2010 [11]. The assumed value of axial tensile strength of concrete f_t was taken as $0.395f_{cu}^{0.55}$ in accordance with GB50010-2010 [11].

All steel rebar used for the wall specimens had a strength grade of HRB400 (nominal yield strength $f_{y,n}$ = 400 MPa), which is commonly-used for building constructions in China. Table 1 summarizes the measured reinforcement yield strength, ultimate strength and uniform elongation (i.e., measured strain corresponding to the peak stress). These are the average values obtained by three standard rebar tensile tests for each type of steel rebar.

Table 1 Material properties of steel rebar used in experimental specimens.

Diameter (mm)	Yield strength f_y (MPa)	Ultimate strength f_u (MPa)	Uniform elongation δ (%)
6	479.2	590.3	16.5

8	426.3	555.2	12.6
10	396.3	555.3	11.4
14	466.7	539.4	7.9

2.2. Axial tensile force

In practical design, the Chinese Technical Guideline of Peer Review for Seismic Design of Super-Tall Buildings [12] stipulated that the ratio of average nominal tensile stress of a section to the tensile strength of concrete f_t shall be less than 1.0 for RC walls under the design basis earthquake (DBE, with a probability of exceedance of 10% in 50 years). Otherwise, the use of steel reinforced concrete (SRC) walls or steel-plate composite walls is recommended [13-16], for enhancement of the wall's strength capacity. Therefore, normalized concrete tensile stress (n_c), as defined in Eq. (1), was used as an indicator to quantify the magnitude of axial tensile force.

$$n_c = \frac{T_n}{\left(A_c + A_s E_s / E_c\right) f_t} \tag{1}$$

where T_n denotes the axial tensile force of the wall, A_c denotes the cross-sectional area of concrete, A_s denotes the cross-sectional area of vertical reinforcement (including vertically distributed rebar and boundary longitudinal rebar), E_s and E_c denote the elastic modulus of steel and concrete, respectively, and f_t denotes the axial tensile strength of concrete.

For $n_c \leq 1$, the value of n_c represents the ratio of nominal axial tensile stress to concrete tensile strength. However, for $n_c > 1$, concrete sustains tensile cracking and the tensile force is carried only by vertical reinforcement at cracked sections. Therefore, normalized reinforcement tensile stress (n_s), as defined in Eq. (2), is proposed as another indicator to quantify the magnitude of axial tensile force [5,8]. Note that n_s = 1 corresponds to the axial tensile yield strength of RC walls.

$$n_s = \frac{T_n}{A_s f_y} \tag{2}$$

where f_y denotes the yield strength of vertical reinforcement.

Table 2 summarizes the values of axial tensile force and the values of n_c and n_s for the four test walls. In the calculation, the measured strengths of concrete and rebar were adopted. The n_s values ranged from 0.23 to 0.91 for the specimens HSW1 through HSW4. The experiment test of a substructure model representative of a modern coupled wall in a 10-story building [5] indicated that the axial tensile force level n_s of the wall piers could reach up to 0.72. Increase of the coupling ratio or structural height of the coupled wall system would lead to further increase of the n_s value of wall piers.

Table 2 Axial tensile force values of RC wall specimens.

Spec. no.	HSW1	HSW2	HSW3	HSW4
T_n / (kN)	322	538	897	1291
n_c	0.33	0.73	0.98	1.73
n_s	0.23	0.38	0.63	0.91

2.3. Test setup

The test setup is shown in Fig. 3. The foundation beam was clamped to the reaction floor and the top beam was clamped to two hydraulic actuators, one in the horizontal direction and the other in the vertical direction. Out-of-plane support was provided to prevent out-of-plane deflections and twisting of the wall specimen during testing.

Two phases of loading were included in the test. The first phase consisted of applying the vertical axial tension to the specimen using the vertical actuator with increments of $0.2T_n$ until the target tensile force T_n was reached. After applying the axial tension, the vertical actuator was controlled to maintain a constant axial tension throughout the testing. The second phase of loading consisted of the cyclic lateral loads that were applied by the horizontal actuator. As shown in Fig. 2, the distance H from the top of the wall base to the centroid of the horizontal actuator was 3000 mm, and thus the aspect ratio (H/L, i.e., shear-to-span ratio) of the wall specimen was equal to 2.0.

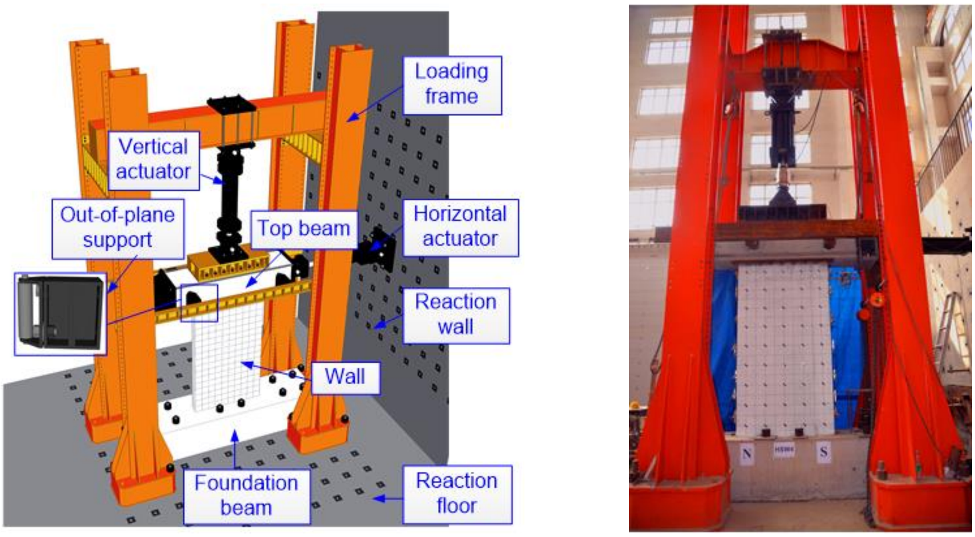

(a) Schematic drawing (b) Photograph

Fig. 3. Test setup.

Fig. 4 shows the history of cyclic lateral loading, which was determined based on the Chinese Specification for Seismic Testing of Buildings (JGJ 101-2015) [17]. In the elastic region, two levels of lateral drift loading were included (0.1% and 0.2%) and one cycle was performed at each level. After the specimen reached the predicted yield drift (i.e., 0.35%), the lateral displacement load was increased at 0.25% increments, and two cycles were repeated at each drift level. In the test, push was defined as positive loading and pull as negative loading, and each push was followed by a pull for each cycle. As per the Chinese code JGJ 101-2015 [17], the test was terminated when the lateral force of the specimen dropped below 85% of the maximum lateral force or the specimen could not sustain the axial tensile force, due to fracture of the vertical reinforcement.

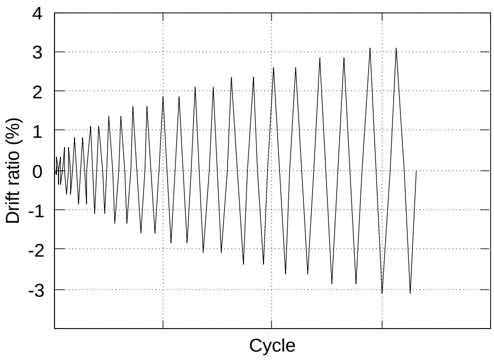

Fig. 4. Cyclic lateral loading history.

It is acknowledged that the loading in this testing scheme, combined with initially applied constant axial tensile forces and increased cyclic lateral loads, may not exactly represent the actual loading condition of walls in a high-rise building. In a couple wall system, the wall pier would be subjected to varied axial tensile forces at different lateral drifts, and the axial forces would change from tension to compression during the lateral drift reversal. Nevertheless, the loading method in this program provides an effective way to examine how different magnitudes of axial tension influence the flexural behavior of the RC walls, which is the main objective of the study. The influence of loading history on the crack pattern and behavior of the walls is out of the scope of this paper and is left for future study.

2.4. Instrumentation

Load cells were used to measure vertical tension and lateral force applied by the actuators. The layout of linear variable differential transformers (LVDTs) mounted on the specimens are shown in Fig. 5(a). LVDT D29 measured the lateral displacement at the centroid of the top beam, which was also used for displacement control of lateral loading. LVDTs D18 through D24 measured lateral displacement distribution along the wall height. Two pairs of inclined LVDTs (D25 through D28) measured the shear deformation of the wall, and fourteen LVDTs (D1 through D14) were mounted along both wall edges to measure flexural deformation of the specimen. Three LVDTs (D33 through D35) were used to monitor possible rotation and slip of the foundation beam. LVDTs D1, D15 to D17, and D8 were used to measure the vertical strain distribution over the cross-section at the wall bottom. LVDT D30 was used to monitor axial elongation at the centroid of the wall top. Out-of-plane deformation was monitored by D31 and D32. In addition, a photogrammetric system using high-solution digital cameras was used for displacement measurement as well. Photogrammetry targets were placed on the full specimen with 300 mm grid spacing, as shown in Fig. 5(b).

Reinforcement strains were measured using thirty strain gauges that were mounted on the distributed rebar, as well as on the boundary longitudinal and transverse rebar, as shown in Fig. 5(c).

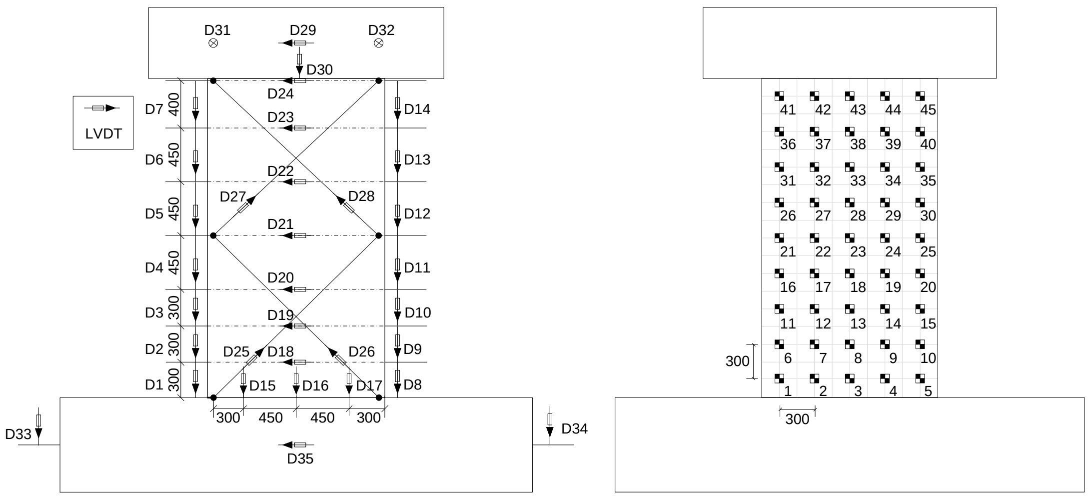

(a) Displacement transducers (b) Photogrammetry targets

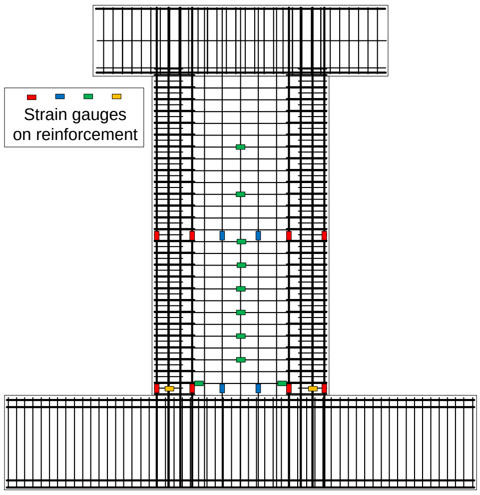

(c) Strain gauges

Fig. 5. Layout of instruments.

3. Experimental results

3.1. Damage and failure modes

Fig. 6 shows the cracking patterns of wall specimens after applying the axial tensile force and prior to any lateral loading. The widest cracks are also identified in this figure. Horizontal thorough cracks were observed in specimens HSW2 through HSW4, while no cracks occurred in HSW1. For specimens HSW2 and HSW3, the wide horizontal cracks mainly appeared in the lower portion of walls and the widest cracks were 0.05 mm and 0.25 mm, respectively. For specimen HSW4, dense horizontal cracks developed along the entire height of wall with a spacing of approximately 150 mm and the widest crack was located at the upper portion of wall with a thickness of 6.5mm. Note that although the value of n_c for specimens HSW2 and HSW3 was less than 1.0 (see Table 2), the wall specimens sustained cracking after the application of axial tensile force. It is because the drying shrinkage effect of concrete was not accounted for the calculation of n_c [8]. As the reinforcement provided the constraint to the concrete shrinkage, the internal tensile stresses developed in the wall concrete. When the total concrete tensile stresses, including the shrinkage tensile stresses and the additional tensile stresses induced by the external tensile force, reached the concrete tensile strength, cracking occurred in the walls.

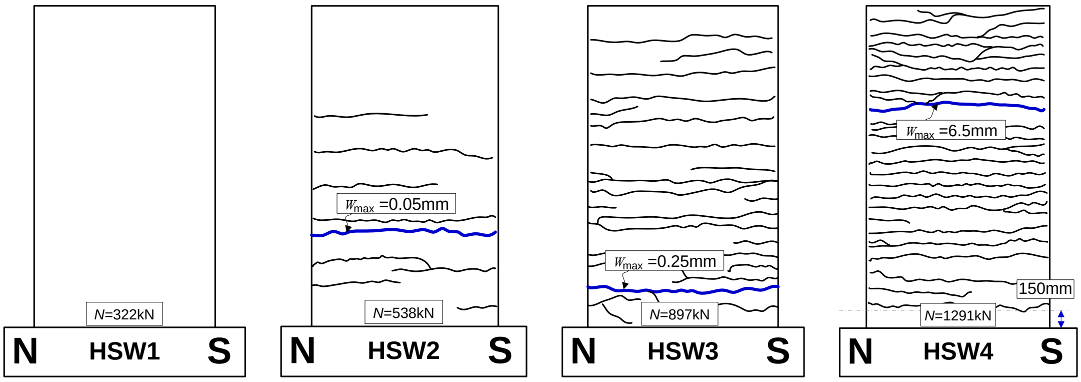

HSW1 HSW2 HSW3 HSW4

Fig. 6. Crack patterns of specimens after applying axial tensile force.

After applying cyclic lateral loading, the initial horizontal cracks widened and some inclined cracks developed from the wall edges extended to the center of wall. Finally, two types of failure modes were observed in the tests: (a) flexural-sliding failure (for specimens HSW1, HSW2 and HSW3) and (b) flexural failure (for specimen HSW4). The crack patterns of the wall specimens at peak lateral load and at the end of testing are shown in Fig. 7 and Fig. 8, respectively.

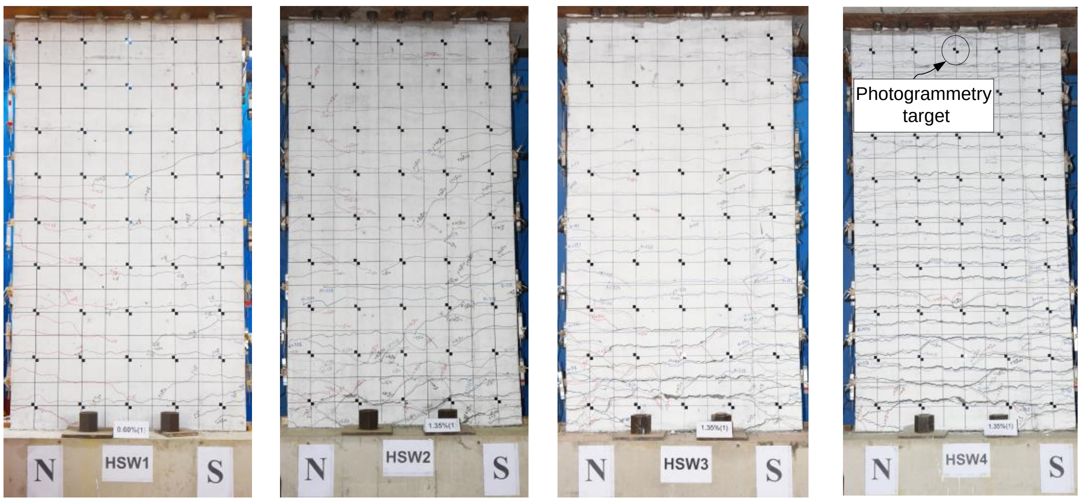

(a) HSW1 (θ = 0.60%) (b) HSW1 (θ = 1.35%) (c) HSW3 (θ = 1.35%) (d) HSW4 (θ = 1.35%)

Fig. 7. Photographs of crack patterns of specimens at peak lateral load.

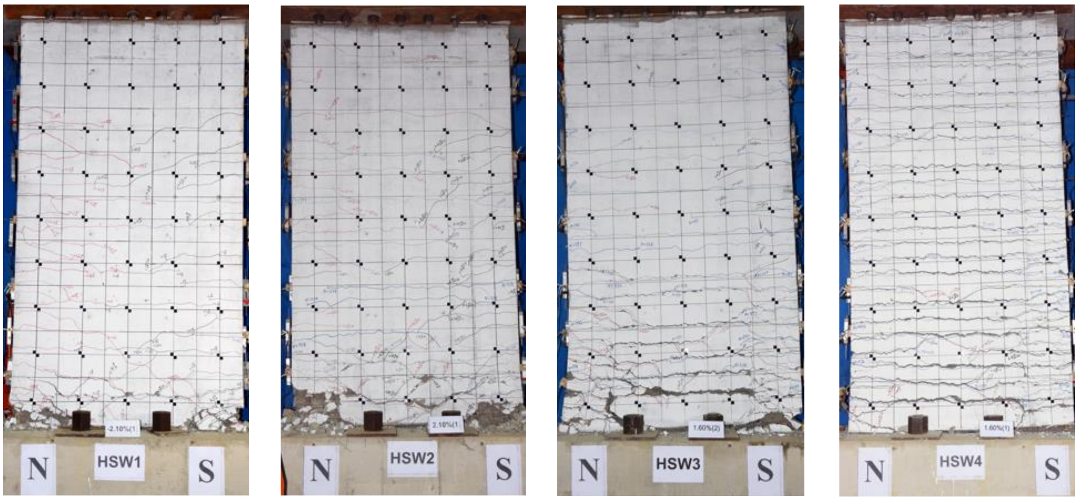

(a) HSW1 (θ= 2.10%) (b) HSW2 (θ= 2.10%) (c) HSW3 (θ= 1.60%) (e) HSW4 (θ= 1.60%)

Fig. 8. Photographs of specimens at end of testing.

Flexural-sliding failure: Specimens HSW1, HSW2 and HSW3 that had the normalized concrete tensile stress n_c<1.0 sustained flexural-sliding failure. The three specimens all failed in a progression of flexural cracking, yielding of vertical reinforcement, spalling of concrete cover, sliding along the wall base surface and fracture of boundary longitudinal rebar. The so-called ‘flexural-sliding failure’ mode is characterized by a transition from initially yielding of the wall ’s boundary longitudinal rebar and vertically distributed rebar mainly induced by flexural deformation to the sliding failure along the critical crack surface. The following describes the observed behavior of HSW3 as an example for illustration of the damage progression and flexural-sliding failure.

The first horizontal flexural crack at the wall boundary was observed at 0.2 % drift. Upon further loading reversal, the boundary longitudinal rebar yielded. Minor spalling of concrete cover at two wall edges adjacent to the wall-foundation block interface occurred at 0.85% drift. Afterwards, all vertical reinforcement yielded under combined flexure and axial tensile demands, and thus horizontal cracks at the wall base widened significantly. At 1.35% drift, an obviously horizontal sliding surface along the wall-foundation block interface was formed. Upon further loading, the wall specimen obviously slid along the sliding surface, and the vertical reinforcement that passed through the sliding surface showed local flexural and kinking deformation (see Fig. 9(a)). Finally, the wall specimen failed due to the fracture of the boundary longitudinal rebar and vertically distributed rebar. It is noted that the reinforcement fracture in specimens HSW1 through HSW3 was due to the local flexural and kinking deformations on the rebar, rather than large tensile strain caused by the bending moment.

Fig. 10 conceptually illustrates the mechanism of flexural-sliding failure. Under small lateral load, flexural deformation dominated the behavior of wall specimen, which was mainly characterized by development of flexural cracks at the wall boundary (Fig. 10 (a)). Upper further cyclic reversal, flexural cracks extended from edges to the wall centroid, and finally developed into a continuous, approximately horizontal, sliding surface at the wall base (Fig. 10(b) and (c)). After the boundary longitudinal rebar yielded, the flexural cracks widened with increased lateral load. The compression zone became smaller, resulting in a decrease in the sliding shear resistance along the sliding surface. When sliding shear resistance decreased below the lateral load, sliding occurred and there was a shift to sliding-dominated behavior (Fig. 10(d)).

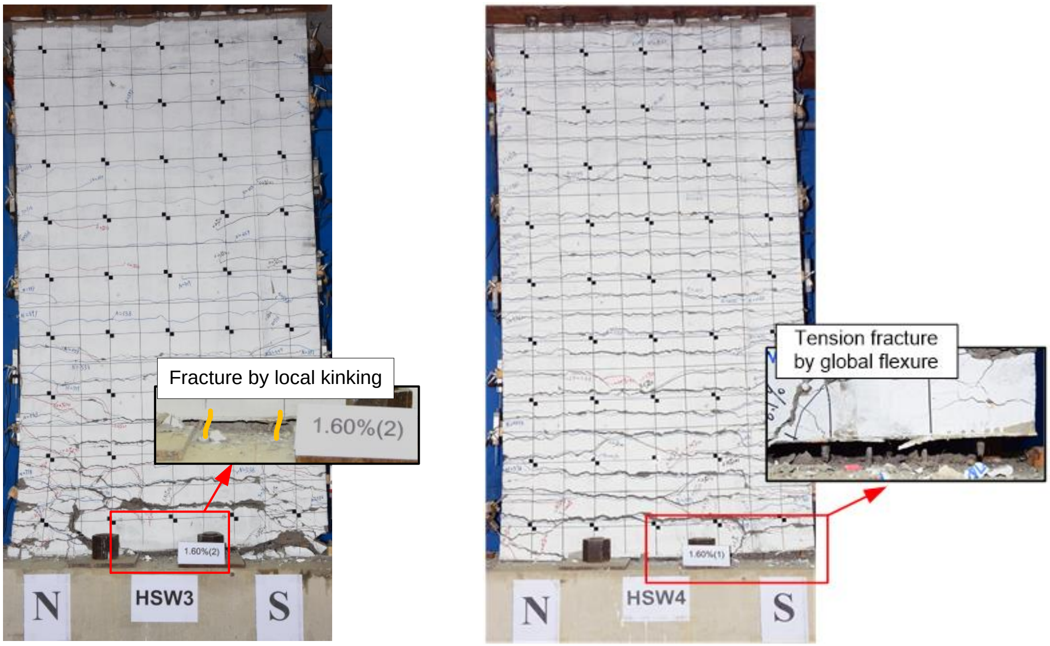

(a) HSW3 (b) HSW4

Fig. 9. Deformation mode of fractured reinforcement for wall specimens.

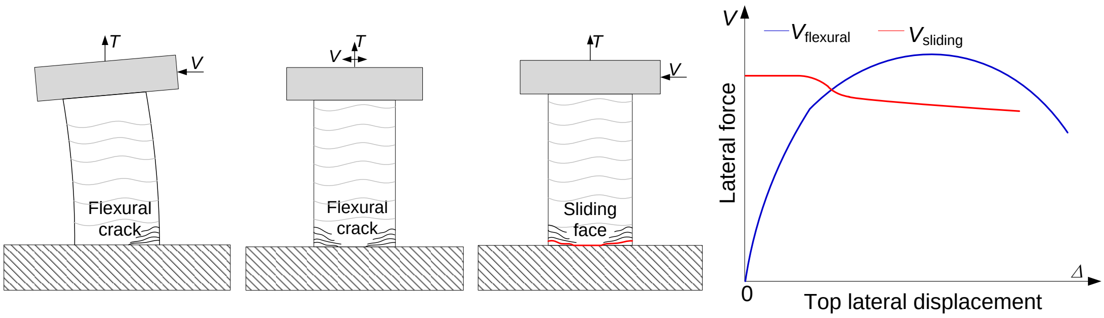

(a) (b) (c) (d)

Fig. 10. Schematic diagrams illustrating the mechanism of flexural-sliding failure.

Flexural failure: Specimen HSW4 that had a normalized concrete tensile stress n_c >1.0 experienced flexural failure characterized by the tensile fracture of boundary longitudinal rebar at the wall base. When applying the lateral loading, the initial horizontal cracks in a region of 600 mm above the wall base significantly widened and new flexural cracks developed at the wall boundary element. Upon further loading, slight sliding was observed along several of the wide horizontal cracks. Ultimately, the boundary longitudinal rebar fractured due to large tensile strain caused by combined flexure and large axial tension demands (see Fig. 9 (b)), which is different from the reinforcement fracture in specimens HSW1 through HSW3 (due to local kinking deformations).

Interestingly, no buckling of vertical rebar was observed in the tests although it often occurred in past tests of RC slender walls subjected to axial compressive force and cyclic lateral loading. Besides, the failure of the specimens was also different from cyclic test observations of some RC walls having no axial load or low level of axial compression load, where the out-of-plane buckling developed in the wall compression boundary [18]. The out-of-plane buckling of wall compressive boundary was due to the distortion of reinforcement under the load reversal from large tensile strains and non-uniform crack closure. In this test program, the axial tensile force remained constant upon load reversal, resulting in the vertical reinforcement kept in tensile strain as indicated by the strain measurement data. It is the major reason why neither buckling of vertical rebar nor out-of-plane buckling of wall compressive boundary occurred in the wall specimens of this test program. However, in a coupled wall system, the axial force of the wall piers would vary from tension to compression during the lateral drift reversal, and the compressive axial force may trigger the buckling of vertical reinforcement or out-of-plane buckling of compressive boundary. Investigation on the influence of axial load variation on seismic behavior of RC walls is needed in future study.

3.2. Lateral load responses

Fig. 11 shows the lateral force versus top displacement hysteresis response, measured by LVDT D29 for four specimens. The points corresponding to the yielding of boundary longitudinal rebar, yielding of vertically distributed rebar and fracture of boundary longitudinal rebar are identified in Fig. 11. The yielding of reinforcement was determined based on the strain gauge data. Note that the strain-gauge measurements indicated that the horizontally distributed rebar and boundary transverse reinforcement did not yield during any of the tests.

In addition, cross-section analysis was conducted using the program XTRACT [19] and the measured material properties of the wall specimen. In the analysis, the concrete confinement effect and strain hardening of reinforcement were considered in the material properties (more details can be found in sub-section 4.3). The calculated shear force corresponding to the wall's flexural yield strength (V_y @ $M_{y,XTRACT}$) and that corresponding to the flexural strength capacity (V_p @ $M_{p,XTRACT}$) using XTRACT section analysis are plotted in Fig. 11 as well. Note that the yield flexural strength $M_{y,XTRACT}$ was determined at the yielding of boundary longitudinal rebar, and the flexural strength capacity $M_{p,XTRACT}$ was determined when the compressive strain of extreme compression fiber reached 0.003.

Four main observations can be made from the lateral load responses in Fig. 11. (1) Specimens HSW1 through HSW3 which were defined as the flexural-sliding failure showed post-peak strength degradation, while specimen HSW4 that was defined as a flexural failure did not show strength degradation till sudden fracture of boundary longitudinal rebar. (2) For specimens HSW1 through HSW3, the longitudinal boundary rebar yielded first, followed by the yielding of vertically distributed rebar. While for specimen HSW4, the vertically distributed rebar yielded earlier than the boundary longitudinal rebar after application of axial tensile force due to the nonuniform axial stress distribution along the wall section. For all specimens, the measured yield strength corresponding to the yield of all boundary longitudinal rebar correlated well with the calculated value from the XTRACT cross-section analysis. (3) For specimens HSW1 through HSW3, the experimental lateral load did not reach the calculated value of the flexural strength capacity which corresponds to the extreme concrete compression fiber strain of 0.003, because the mechanism transition from the flexure to sliding impeded the full development of the flexural strength capacity of the walls. However, specimen HSW4 which failed in the flexural mode developed its strength approaching to the flexural strength capacity calculated by XTRACT. (4) Specimens HSW1, HSW2 and HSW3, showed somehow pinching in hysteresis loop, which is suspected to be related to the opening and closure of flexural cracks. However, no pinching was observed in specimen HSW4, as the horizontal cracks in specimen HSW4 did not completely close under the lateral loading reversal and its hysteresis response was mainly controlled by vertical reinforcement.

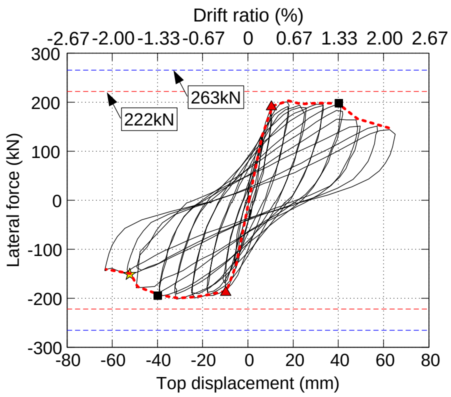

(a) HSW1

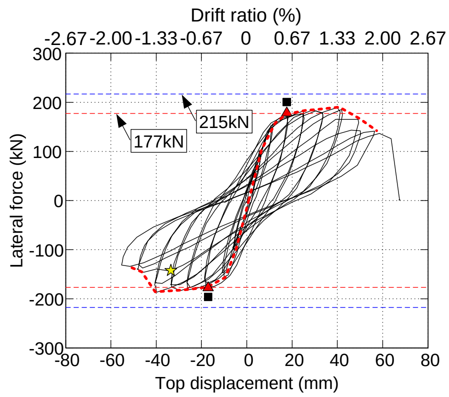

(b) HSW2

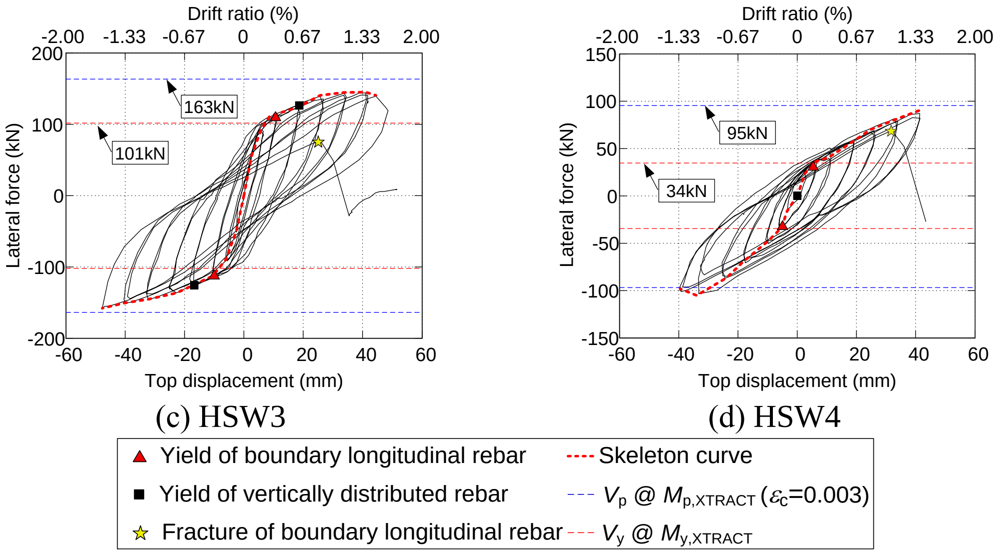

Fig. 11. Lateral force versus top displacement response for all test walls.

3.3. Lateral strength and deformation capacities

Table 3 summarizes the measured yield strength (V_y) and corresponding yield drift (Δ_y), the peak lateral strength (V_p) and corresponding drift (Δ_p), and the ultimate drift (Δ_u) and corresponding drift ratio (θ_u). The yield point corresponds to the yielding of boundary longitudinal rebar and it was determined using the strain measurement data. The ultimate drift is defined as the post-peak drift at the instant when the lateral load decreases to 85% of the peak load [17]. For specimens HSW3 and HSW4, the post-peak strength did not decrease below 85% of the peak load till failure (i.e., loss of axial tensile strength capacity due to rebar fracture). In such a case, the ultimate drift is defined as the maximum drift that the specimen endures with a full cycle before failure. The ultimate drift ratio is calculated as $\theta_u = \Delta_u / H$, where H is the height of the LVDT D29 relative to the wall base. The values of θ_u shown in Table 3 are the average values measured during the positive and negative loading.

The data presented in Table 3 indicate that applied axial tension significantly influenced the lateral strength capacity of the wall specimens. The maximum lateral strength of specimen HSW1 (n_c = 0.33) was larger than that of HSW4 (n_c = 1.73) by 59%. All specimens that failed in flexural-sliding mode exhibited consistent ultimate drift ratio of 1.6%. The ultimate drift of specimen HSW4 that failed in flexural mode was 1.3%, approximately 20% smaller than that of the other specimens.

Table 3 Lateral strength and deformation capacities of test walls.

Spec. no	Direction	Δ_y/mm	V_y/kN	Δ_p/mm	V_p/kN	Δ_u/mm	θ_u
HSW1	N+	10.3	189.5	17.3	200.2	46.0	1.6%
	S-	-10.0	-187.4	-17.7	-195.3	-50.2	
HSW2	N+	10.8	157.8	39.9	189.1	50.5	1.6%
	S-	-11.6	-156.6	-39.8	-187.2	-43.7	
HSW3	N+	8.7	110.3	41.1	143.9	48.6	1.6%
	S-	-10.4	-112.6	-47.7	-157.0	-47.7	
HSW4	N+	5.7	34.3	41.3	86.8	41.3	1.3%
	S-	-5.1	-33.3	-33.0	-103	-38.7	

3.4. Deformation analysis

The deformation components, including flexural, shear and sliding deformations, were calculated using measurements from the photogrammetric system. The accuracy of the photogrammetric system was validated by comparison with the LVDT measurement data. An example is shown in Fig. 12, where the photogrammetric measurement tracked well with the LVDT data for the lateral top displacement of specimen HSW2, with an error of 6%. The flexural and shear deformations at different locations along the height of the wall were calculated from the relative movement of two adjacent rows of photogrammetry targets. The flexural deformations were computed by integrating the rotations calculated from these measurements along the wall height. The shear deformations were computed for each region bordered by four targets using the method proposed by Massone and Wallace [20]. The sliding deformation developed at wall base was calculated by averaging the horizontal displacement of the lowest row of photogrammetry targets which were set at 150 mm height above the wall base. The contributions of flexural and shear deformations to the horizontal displacement at the 150 mm height was negligible compared to the sliding deformation, once the base sliding occurred.

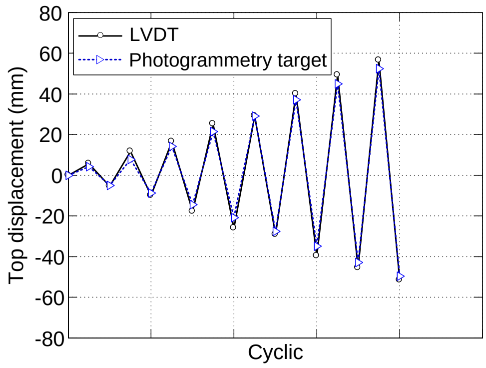

Fig. 12. Validation of photogrammetric system measurement for HSW2.

Fig. 13 shows the contributions of flexural, shear and sliding deformations for specimens HSW1 through HSW4. The following observations can be obtained from the results shown in Fig. 13: (1) Prior to the yielding, flexural deformations dominated the response, exceeding 85% of the total lateral displacement for all specimens. (2) For the specimens HSW1 through HSW3 that failed in flexural-sliding mode, obvious base sliding occurred after flexural yielding of the walls. The base sliding deformation contributed to 58%, 52% and 20% for the top lateral displacement at failure of specimens HSW1, HSW2 and HSW3, respectively. However, specimen HSW4 that failed in a flexural mode showed no base sliding deformation. (3) After flexural yielding, significant shear deformations were developed for all specimens, although the nominal shear strength of the walls calculated per Chinese code JGJ 3-2010 formulas was approximately 1.5 times larger than the applied maximum lateral shear forces. The shear deformation contributed to 19%, 20%, 51% and 28% for specimens HSW1 through HSW4 at failure, respectively. This is due to the shear-flexural interaction, where the inelastic flexural deformations of walls led to inelastic shear deformations developed in plastic hinge region. Similar observations of shear-flexural interaction were found for the tests by Massone and Wallace [20], where the slender RC wall specimens with the shear-to-span ratio of 3.0 were subjected to combined axial compression (axial force ratio = 0.10) and lateral cyclic loading.

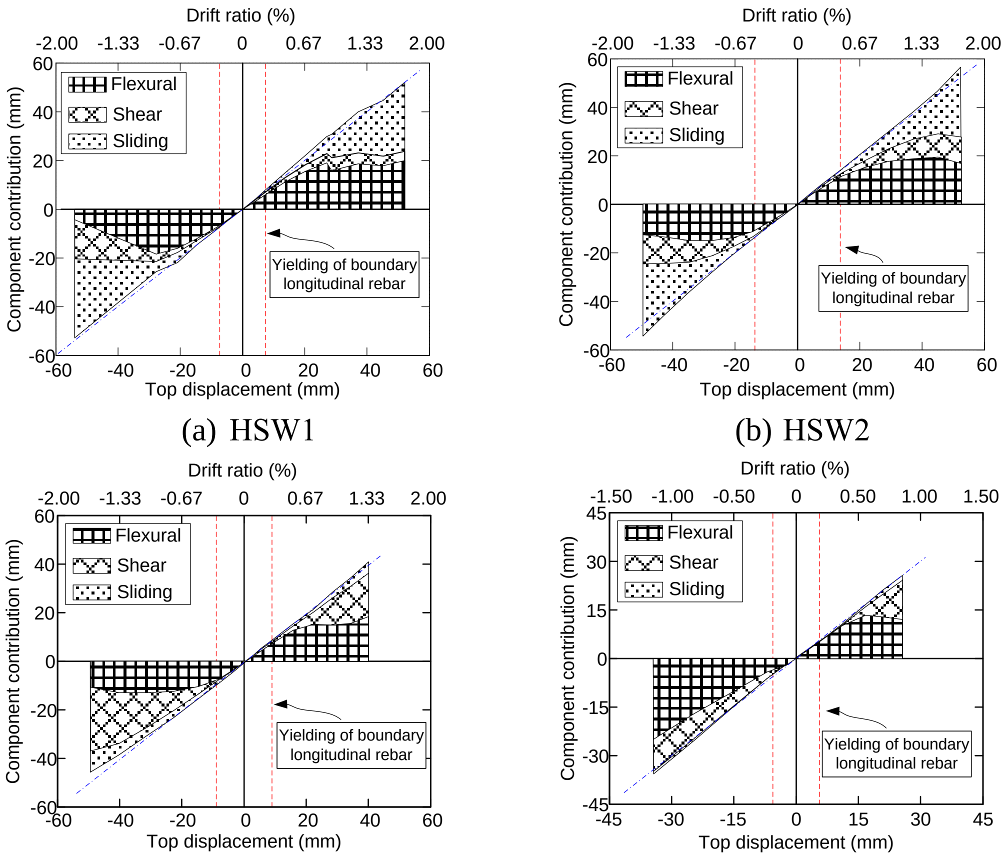

(a) HSW1 (b) HSW2

(c) HSW3 (d) HSW4

Fig. 13. Deformation contributions of wall specimens

4. Theoretical analysis and design recommendations

4.1 Effective flexural stiffness

The effective flexural stiffness EI_{eff} is one of the key design parameters of the walls used for linear response spectrum analysis. The effective flexural stiffness is determined using the idealized force-displacement curve method in accordance with ASCE/SEI 41-13[21], which is smaller than the gross flexural stiffness EI_g due to the effect of concrete cracking and bond slip. Table 4 summarizes the equations for calculation of effective stiffness for RC cracked walls. ACI 318-14 [9] and ASCE/SEI 41-13 [21] recommend $0.35EI_g$ and $0.50EI_g$ for cracked concrete section, respectively. Paulay & Priestley [22] recommend the effective stiffness shown in Eq. (5), where the effective stiffness linearly increases with an increase in the axial compressive force ratio. Adebar et al. [23] recommend the upper and lower bounds of effective flexural stiffness, which also take into account the effect of axial compressive force ratio shown in Eq. (6). While these equations have been compared and validated with test data of walls under combined flexure and axial compressive load [14], it is not clear whether these equations can be extended to use for RC walls under combined flexure and axial tensile demands.

Table 4 Effective flexural stiffness for cracked RC wall.

ACI 318-14 [9]	$(EI)_{eff} = 0.35EI_g$	(3)
ASCE/SEI 41-13 [21]	$(EI)_{eff} = 0.50EI_g$	(4)
Paulay & Priestley [22]	$(EI)_{eff} = \left(\frac{100}{f_y} + \frac{N}{f_c A_g}\right) EI_g < EI_g$	(5)

Adebar et al. [23]	$(EI)_{\text{eff}}=\begin{cases}(0.6+N/f_{c}A_{g})EI_{g}\le EI_{g} \\ (0.2+2.5N/f_{c}A_{g})EI_{g}\le 0.7EI_{g}\end{cases}$	Upper-bound Lower-bound	(6)

Note: f_y denotes the yield strength of longitudinal rebar; EI_g denotes the gross flexural stiffness of wall section; f_c denotes axial compressive strength of concrete; A_g denotes gross cross-sectional area; N denotes the axial force. The sign of N is defined as positive for compression and negative for tension in Eqs. (5) and (6) and Fig 14, which is different from the rest of this paper.

Fig. 14 shows the relationship of effective flexural stiffness normalized with gross flexural stiffness EI_g versus axial force ratios $N/(f_cA_g)$. The following observations can be obtained from Fig. 14: (1) The effective stiffness of wall sections decreased as the axial tensile force increased. For specimen HSW1 ($N/(f_cA_g)$ = -0.009), the effective flexural stiffness $EI_{\text{eff}} = 0.10EI_g$, while for HSW4 ($N/(f_cA_g)$= -0.19), $EI_{\text{eff}} = 0.018EI_g$. (2) ACI 318-14 and ASCE/SEI 41-13 codes overestimated the effective flexural stiffness of RC walls under the combined flexure and axial tensile load by a considerable amount. (3) The equation proposed by Paulay & Priestley (Eq. (5)) captured the general trend of effective flexural stiffness variation with axial tensile forces, but still overestimated the effective flexural stiffness. (4) Although all test data fell into the region between the upper and lower bounds recommended by Adebar et al., there was large uncertainty between those two bounds. Therefore, it is necessary to accumulate more test data and further develop the formulas for effective flexural stiffness of RC walls subjected to axial tensile load.

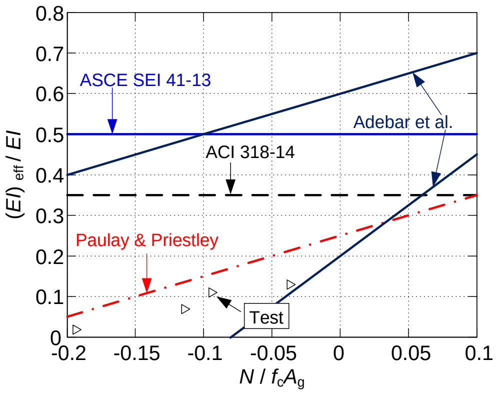

Fig. 14. Evaluation of effective flexural stiffness of RC tensile walls.

4.2. Validation of flexural strength design

Leading design codes (e.g., ACI 318-14 (U. S.), Eurocode 8 (Europe) [24], GB 50010-2010 (China), NZS 3101:2006 (New Zealand) [25]) specify a standard sectional calculation for nominal flexural strength of RC members. The sectional calculation follows the assumptions: (1) Plane sections remain plane after bending; (2) The maximum strain at the extreme concrete compression fiber is assumed equal to 0.003 (ACI 318-14, NZS 3101:2006) or 0.0033 (GB 50010-2010); (3) Tensile strength of concrete is neglected; (4) The stress-strain relationship of steel is represented by a bilinear model, neglecting the strain hardening effect; and (5) The relationship between concrete compressive stress and strain is represented by a rectangular, trapezoidal, parabolic, or other reasonable shape. The equivalent rectangular stress block can be used to calculate the contribution of compressive concrete. However, in order to reduce the iterations required to calculate the flexural strength of members with distributed reinforcement, sectional analysis software (e.g., XTRACT) is often implemented to design RC walls.

Except for the standard sectional calculation, JGJ 3-2010 (China) [10] provides simplified equations to calculate the strength of RC rectangular walls under combined flexure and axial tensile load. These equations use linear plots to approximate the *M-N* interaction diagram in the tension-flexure domain, given by:

$$\frac{N}{N_\mathrm{u}}+\frac{M}{M_\mathrm{u}}=1 \tag{7}$$

$$N_\mathrm{u}=2f_\mathrm{y}A_\mathrm{s}+f_\mathrm{yw}A_\mathrm{sw} \tag{8}$$

$$M_\mathrm{u}=f_\mathrm{y}A_\mathrm{s}\left(h_\mathrm{w0}-d_\mathrm{c}\right)+f_\mathrm{yw}A_\mathrm{sw}\frac{\left(h_\mathrm{w0}-d_\mathrm{c}\right)}{2} \tag{9}$$

where N and M denote the axial tensile force and bending moment in a wall section, N_u denotes the axial tensile yield strength, M_u denotes the pure flexural strength without application of axial forces, f_y denotes the yield strength of boundary longitudinal reinforcement, A_s denotes the cross-sectional area of longitudinal reinforcement in one boundary element, f_yw denotes the yield strength of vertically distributed reinforcement, A_sw denotes the cross-sectional area of vertically distributed reinforcement, h_w0 denotes the effective depth of wall section, and d_c denotes the depth from the extreme concrete compression fiber to the centroid of compressive boundary longitudinal rebar.

Fig. 15 (a) and (b) plot the normalized *M-N* interaction diagram for the test wall section, obtained from XTRACT analysis and JGJ 3-2010 equations respectively. The test values of yield and peak flexural strength for all specimens are also plotted in the figure. Note that in the calculation of the wall's nominal flexural strength, the XTRACT model satisfied the assumptions specified in ACI 318-14 code for standard sectional calculation, and the concrete confinement effect and strain hardening of reinforcement were not considered. The JGJ 3-2010 equations provides similar prediction of the wall's flexural strength as the sectional analysis result by XTRACT. The calculated flexural strength by XTRACT analysis and per JGJ 3-2010 equations correlates well with the test yield strength, expect for specimen HSW1. Both the XTRACT analysis and JGJ 3-2010 equations obviously underestimate the maximum flexural strength of specimen HSW4. It is because the hysteretic response of specimen HSW4 with high axial tension (n_c = 1.73) is dominated by cyclic behavior of vertical reinforcement, and cyclic hardening of rebar results in a high flexural overstrength which is not reflected in the sectional analysis and design code equations.

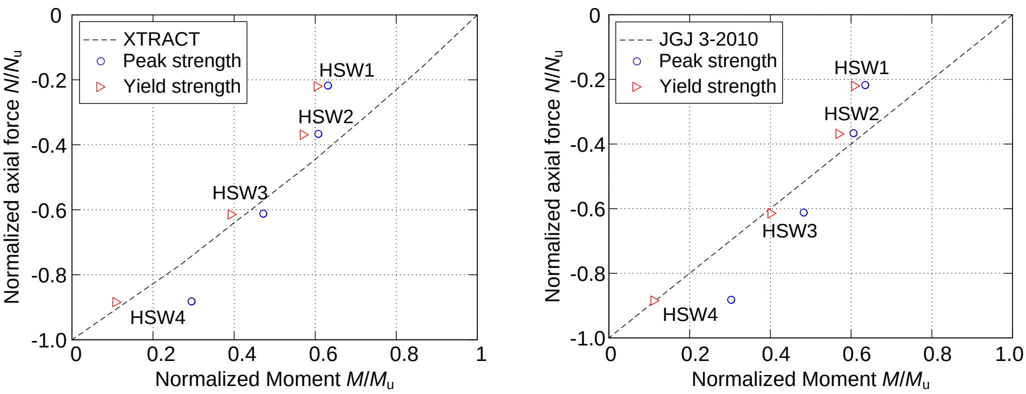

(a) XTRACT sectional analysis (b) JGJ 3-2010 equations

Fig. 15 Verification for flexural strength design.

4.3. Moment-curvature

The relationship of bending moment versus curvature of RC wall sections can be estimated using the cross-section analysis program XTRACT [19], which uses a fiber model. The wall section is shown in Fig. 16. Different uniaxial stress-strain relationships for the concrete, as shown in Fig. 17(a), were used for boundary element and web wall, to reflect the confinement effect provided by transverse reinforcement. The Kent-Park model [26] was used to simulate the compressive uniaxial stress-strain relationship of cover concrete and web wall concrete, where the peak strain was assumed to be 0.002. The residual compressive strength was taken to be 0.2 times the peak strength of concrete. The stirrup confined concrete at the boundary element was represented by the Saatcioglu-Razvi model [27], which takes into account the increase of the strength and ductility of concrete as a result of the confinement effect. The residual compressive strength was also taken to be 0.2 times the peak strength of the concrete.

The uniaxial stress-strain curves of rebar proposed by Esmaeily and Xiao [28] was used for the XTRACT analysis, given by (as shown in Fig. 17(b)).

$$\sigma=\begin{cases} E_{\mathrm{s}}\varepsilon & \left(0 < \varepsilon \leqslant \varepsilon_{\mathrm{y}}\right) \\ f_{\mathrm{y}} & \left(\varepsilon_{\mathrm{y}} < \varepsilon \leqslant k_1 \varepsilon_{\mathrm{y}}\right) \\ k_4 f_{\mathrm{y}} + \dfrac{E_{\mathrm{s}}(1-k_4)}{\varepsilon_{\mathrm{y}}(k_2-k_1)^2}(\varepsilon - k_2\varepsilon_y)^2 & \left(\varepsilon > k_1 \varepsilon_{\mathrm{y}}\right) \end{cases} \tag{10}$$

where f_{y} denotes the yield strength of rebar; E_{s} denotes Young's modulus of steel rebar; ε_{y} denotes the yield strain; k_1 denotes the ratio of the strain at the initiation of hardening to the yield strain, k_2 denotes the ratio of strain at the peak stress to the yield strain, and k_4 denotes the ratio of the ultimate strength to the yield strength. The values of k_1, k_2 and k_4 were determined as the average values obtained from the monotonic stress-strain curves of standard rebar tensile tests, as shown in Fig. 17(c) and (d). The analytical stress-strain curves using Eq. (10) are also plotted in these figures, which matched well with the rebar tensile test results.

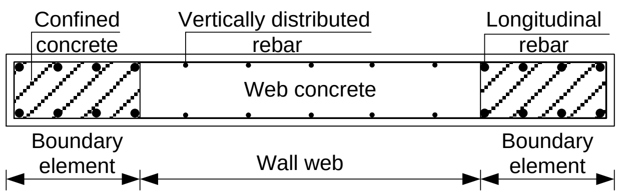

Fig. 16. Sections of wall specimens in XTRACT.

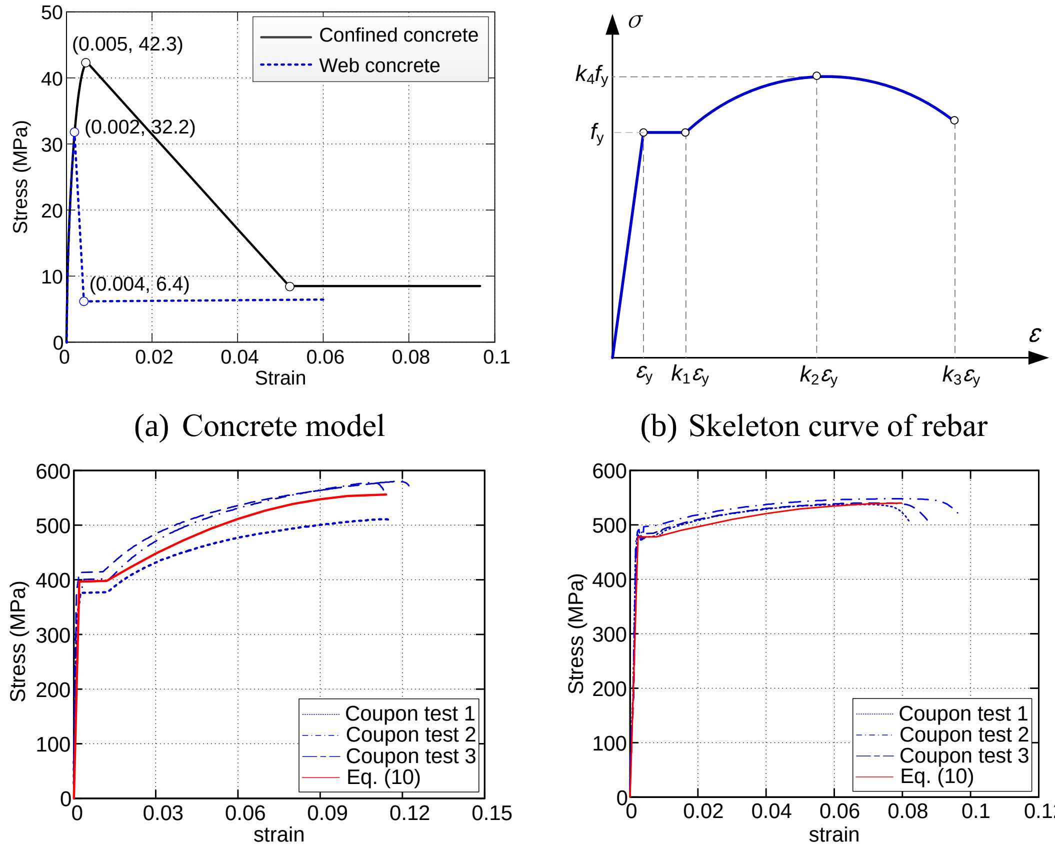

(a) Concrete model (b) Skeleton curve of rebar

(c) D10 rebar (d) D14 rebar

Fig.17. Strain-stress relation of materials in XTRACT.

Fig. 18 shows the moment-curvature response predicted using the program XTRACT, compared with the experimental responses of specimens HSW1 through HSW4. The experimental moment corresponds to the wall base, and it is calculated from the applied lateral force. The experimental curvature is the average curvature over the lower 300 mm of the wall, which is calculated by the value obtained from LVDTs D1 and D8 (as shown in Fig. 5(a)). The effective flexural stiffness EI_{eff} obtained from the analytical moment-curvature curves is approximately 30% higher than the test values. The reason of overestimation of effective flexural stiffness is likely because the sectional analysis does not consider the influence of local deformation induced by concrete crack opening and reinforcement bond slippage at the wall base. The analytical yield strength corresponding to the yield of boundary longitudinal rebar appears to correlate well with the test results. After the yield of boundary longitudinal rebar, for specimens HSW1 through HSW3, the analytical lateral strengths is higher than the experimental strength, because the sliding observed in the tests impedes the full development of the flexural strength capacity of the walls. For the three wall specimens, the experimental curvature in the positive direction is larger than the negative direction for the sliding deformation mainly occurred in the negative direction. For specimen HSW4, the analytical yield strength is similar as the test value, while the XTRACT analysis significantly underestimates the post-yielding strength development. It is because the monotonic-load analysis cannot reasonably represent the cyclic hardening of rebar. It is noted that the experimental curvature of specimen HSW4 may not be accurate, because the vertical displacement measurements at wall base indicates that the plane-section assumption is not satisfied for this wall under high axial tension.

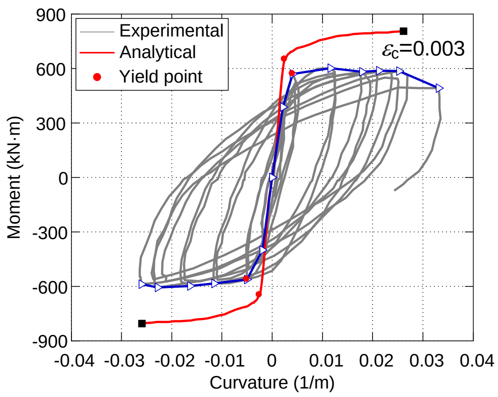

(a) HSW1

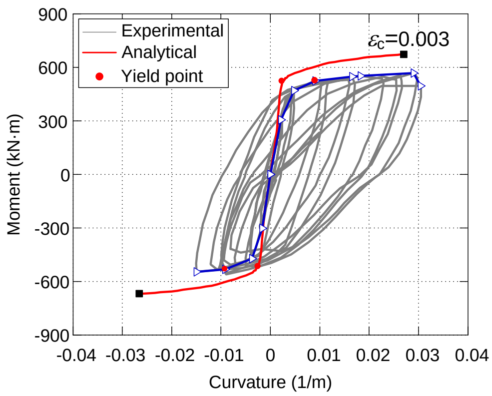

(b) HSW2

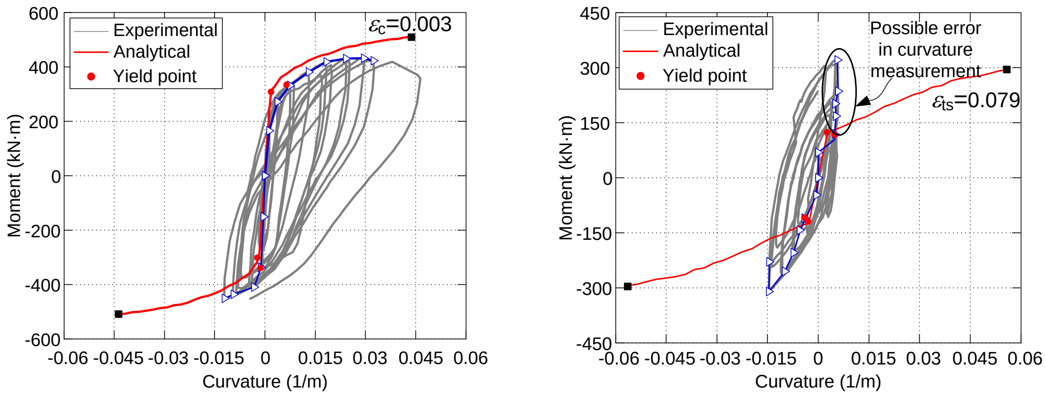

(c) HSW3 (d) HSW4

Fig. 18. Moment versus curvature for specimens.

5. Axial elongation

5.1. Measured axial elongation

The high axial elongation of RC walls is of particular interest, especially at the loading stage of combined axial tension and cyclic lateral loading. Fig. 19 shows the relationship of axial elongation at the centroid of the wall top versus lateral displacement peaks for specimens HSW1 through HSW4. Note that, the wall axial elongation data for specimen HSW1 through HSW3 were directly measured by the vertical LVDT 30 (as shown in Fig. 5). The axial elongation of HSW4 was measured by photogrammetric system, because the LVDT 30 installed in this specimen dropped during the testing. Fig. 19 indicates that the axial elongation appears to linearly increase as displacement increases for all walls, with factors of 0.48, 0.67, 1.28 and 2.31 for specimens HSW1 through HSW4, respectively. These factors increases along with an increase in the normalized reinforcement tensile stress of the wall specimens. It is also noted that specimen HSW4 has axial elongation initially after application of the high-level of axial tensile force due to yielding of vertical reinforcement, which is different from other three specimens.

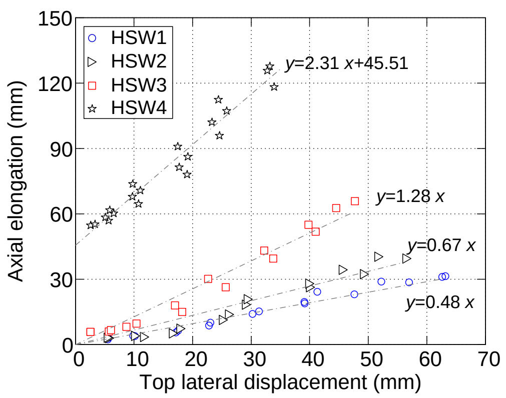

Fig. 19. Axial elongation versus lateral displacement for specimens.

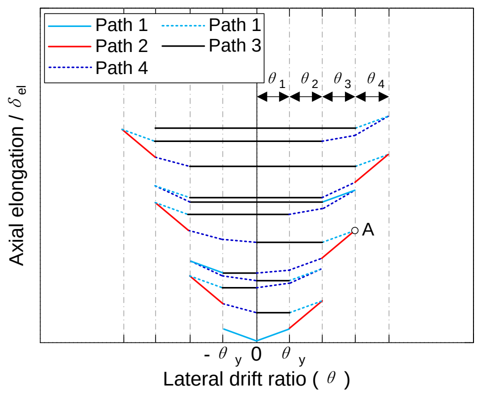

Fig. 20. Analytical model for calculation of axial elongation of RC walls.

5.2. Models for predicting axial elongation

In recent years, the axial elongation of RC walls has received attention in both research and design. In New Zealand Concrete Structures Standard (NZS 3101:2006), an estimate for the axial elongation at the ultimate limit state has recently been introduced based on geometrical relationship assuming that the accumulation due to cyclic loading is minimal for RC walls subjected to axial compressive load [25]. This procedure was confirmed by Encina at al. who compared the estimated elongations against the measured elongations from a number of RC wall tests [29]. Matthews et al. [30] provided a prediction of RC beam elongation under cyclic loading using a rainflow method. Based on the experimental characteristics of wall elongation, Lee & Watanabe [31] proposed a simplified model to predict the axial elongation in the plastic region, which considers the influence of loading, unloading and reloading. Jensen [32] proposed a more accurate design model by incorporating loading dependent nature of axial elongation as described in the Lee & Watanabe model [31] into the rainflow method.

The Lee &Watanabe model was used to analyze the test wall elongation response.

In the model, the axial elongation includes four path types (as shown in Fig. 20). (1) Path 1: Pre-flexural yield and unloading region, which describes elastic axial elongation at loading stage and recoverable elastic axial elongation at unloading stage; (2) Path 2: Post-flexural yield region, where axial elongation is generated due to plastic rotation; (3) Path 3: Slip region; and (4) Path 4: Repeated loading region, where axial elongation is accumulated upon repeated rotation cycles and the extent of which is described as decreasing approximately inversely proportional to the number of repeated cycles.

Therefore, the cumulative axial elongation of wall under the reversed cyclic loading δ_{el} can be calculated as follow [31]:

$$\delta_{\mathrm{el}}=\delta_{\mathrm{Path\ 1}}+\delta_{\mathrm{Path\ 2}}+\delta_{\mathrm{Path\ 3}}+\delta_{\mathrm{Path\ 4}} \tag{11}$$

where $\delta_{\mathrm{Path\ 1}}$, $\delta_{\mathrm{Path\ 2}}$, $\delta_{\mathrm{Path\ 3}}$ and $\delta_{\mathrm{Path\ 4}}$ denote the cumulative axial elongation at Path 1, Path 2, Path 3 and Path 4, respectively.

By assuming the decreased rate in axial elongation at unloading stage is the same as the increasing rate of axial elongation in the elastic region. The cumulative axial elongation at the Path 1 ($\delta_{\mathrm{Path\ 1}}$) can be calculated as follows [31]:

$$\delta_{\mathrm{Path\ 1}}=(1-F)\ \delta_{\mathrm{y}} \tag{12}$$

$$\delta_{\mathrm{y}}=\left(\frac{h/2-c}{d-c}\right)\varepsilon_{\mathrm{y}}\, l_{\mathrm{n}} \tag{13}$$

where F denotes the number of unloading cycles beyond flexural yielding, δ_{y} denotes the axial elongation at the instant of flexural yielding, h denotes the overall depth of wall section, c denotes the neutral axis depth at the flexural yield point, d denotes the effective depth of section, ε_{y} denotes the yield strain of tensile rebar, and l_{n} denotes the length of plastic hinge region which is taken as $0.5h$.

In order to simplify the calculation, the value of neutral axis depth c can be calculated using Eq. (14) [33]. It is noted that this equation does not consider the influence of axial tensile force.

$$c = n_{\mathrm{E}}\rho_{\mathrm{l}}\left(\sqrt{(1+r)^2 + \frac{2}{n_{\mathrm{E}}\rho_{\mathrm{l}}}\left(1+r\frac{d_{\mathrm{c}}}{d}\right)} - (1+r)\right)h \tag{14}$$

where n_{E} denotes the ratio of elastic modulus of steel and concrete, ρ_{l} denotes the ratio of tensile boundary longitudinal reinforcement, r denotes the ratio of sectional areas of compressive and tensile reinforcement, and d_{c} denotes the depth from the extreme concrete compression fiber to the center of compression reinforcement.

The cumulative axial elongation at the Path 2 ($\delta_{\mathrm{Path\ 2}}$) can be calculated using Eq. 15 [31]:

$$\delta_{\mathrm{Path\ 2}} = (\left|\theta_{\mathrm{p}}^{+}\right| + \left|\theta_{\mathrm{p}}^{-}\right|)\frac{d^{'}}{2} \tag{15}$$

Where θ_{p}^{+} and θ_{p}^{-} denote the positive and negative plastic rotations for one cycle respectively, $d^{'}$ denotes the depth between the centroids of compression and tension reinforcement.

The cumulative axial elongation at the Path 3 ($\delta_{\mathrm{Path\ 3}}$) can be neglected due to an opposing and similar magnitude change in compression and tension reinforcement of a wall. Therefore, the value of $\delta_{\mathrm{Path\ 3}}$ can be calculated using Eq. (16) [31]:

$$\delta_{\mathrm{Path\ 3}} = 0 \tag{16}$$

The cumulative axial elongation at the Path 4 ($\delta_{\mathrm{Path\ 4}}$) can be calculated using Eq. (17).

$$\delta_{\mathrm{Path\ 4}} = \sum_{i=1}^{m}\left[\sum_{j=1}^{N_j}\left(\frac{\theta_i d^{'}}{2l_{\mathrm{n}}}\right)^{0.85}\frac{l_{\mathrm{n}}}{4j}\right] \quad (1 \leqslant N_j \leqslant 5) \tag{17}$$

where θ_i denotes the i_{th} rotation component and N_j denotes the number of the reload for rotation component θ_i. Point A (as shown in Fig. 20) is used to explain Eq. (17). The rotation of Point A can be divided into three components: θ_1, θ_2 and θ_3. The values of N_j corresponding to θ_1 through θ_3 are 4, 3 and 0. Hence, the cumulative axial elongation of Point A at the path 4 can be calculated as follows:

$$\begin{aligned}\Delta_{\text{Path 4}} &= \sum_{i=1}^{m}\left[\sum_{j=1}^{N_j}\left(\frac{\theta_i d'}{2l_{\text{n}}}\right)^{0.85}\frac{l_{\text{n}}}{4j}\right] \\ &= \left(\frac{\theta_1 d'}{2l_{\text{n}}}\right)^{0.85}\frac{l_{\text{n}}}{4}\left(1+\frac{1}{2}+\frac{1}{3}+\frac{1}{4}\right)+\left(\frac{\theta_2 d'}{2l_{\text{n}}}\right)^{0.85}\frac{l_{\text{n}}}{4}\left(1+\frac{1}{2}+\frac{1}{3}\right)\end{aligned} \tag{18}$$

Using the Eqs. (11) through (17), the elongation of RC wall under the cyclic lateral load can be estimated using Eq. (19).

$$\delta_{\text{el}} = [1-F]\Delta_{\text{y}} + \left(\left|\theta_{\text{p}}^{+}\right|+\left|\theta_{\text{p}}^{-}\right|\right)\frac{d'}{2} + \sum_{i=1}^{m}\left[\sum_{j=1}^{N_j}\left(\frac{\theta_i d'}{2l_{\text{n}}}\right)^{0.85}\frac{l_{\text{n}}}{4j}\right] \tag{19}$$

5.3. Refined model for RC wall elongation

In all existing models for wall elongation, the effect of axial force on the axial elongation was considered by the depth of the compressive zone, with consideration mostly to members subjected to axial compression loads. If a modest axial compression load is applied to an RC wall, the axial force is sufficient to close flexural cracks on load reversal, and thus the magnitude of axial compression has little effect on the cyclic axial elongation [29]. However, axial tensile force can significantly increase axial elongation and this has not been considered in previous models or calculations.

To accurately evaluate the axial elongation of RC walls subjected to axial tension and cyclic lateral loading, the model proposed by Lee &Watanabe [31] is further developed to consider the influence of axial tensile force. Based on the experimental observations, these following assumptions are used in this refined model: (1)

Recoverable elastic axial elongation at the path 1 should be reduced, as the axial elongation does not completely recover at the unloading stage for presence of constant axial tensile load. (2) The axial elongation at the loading stage (Path 2) and reloading stage (Path 4) shall be increased to allow for the effect of axial tensile force.

For the presence of constant axial tensile force, the recoverable elastic axial elongation is assumed to be (1-n_s)δ_y, where n_s denotes the normalized reinforcement tensile stress as discussed in section 2.2. Therefore, the cumulative axial elongation of Path 1 ($\delta_{\text{Path 1}}$) can be calculated using Eq. (20):

$$\delta_{\text{Path 1}}=\left[1-F\left(1-n_{\text{s}}\right)\right]\delta_{\text{y}} \tag{20}$$

The axial elongation at path 2 and path 4 is assumed to be amplified by (1+α) times due to the effect of axial tensile load. The factor α equals to the ratio of axial elongation caused by axial tensile force $\delta(N)$ to that caused by flexural deformation $\delta(M)$. If assuming that the factor α is approximate to the ratio of tensile strain of boundary longitudinal rebar caused by the axial tensile force to that caused by bending moment at the yield point, the value of α can be calculated as follows:

$$\alpha=\frac{\delta\left(N\right)}{\delta\left(M\right)}=\frac{n_{\text{s}}\varepsilon_{\text{y}}}{(1\text{-}n_{\text{s}})\varepsilon_{\text{y}}}=\frac{n_{\text{s}}}{1-n_{\text{s}}} \tag{21}$$

Therefore, the cumulative axial elongation at the Path 2 and path 4 can be calculate using Eqs. (22) and (23).

$$\delta_{\text{Path 2}}=\left(1+\alpha\right)(\left|\theta_{\text{p}}{}^{+}\right|+\left|\theta_{\text{p}}{}^{-}\right|)\frac{d'}{2} \tag{22}$$

$$\delta_{\text{Path 4}}=\left(1+\alpha\right)\sum_{i=1}^{m}\left[\sum_{j=1}^{N_j}(\frac{\theta_i d'}{2l_{\text{n}}})^{0.85}\frac{l_{\text{n}}}{4j}\right]\quad(1\leqslant N_{\text{j}}\leqslant 5) \tag{23}$$

Using the Eqs. (20) through (23), the axial elongation of RC walls under axial tensile force and cyclic lateral loading can be estimated as follows:

$$\delta_{\mathrm{el}} = \left[1 - F\left(1 - n_{\mathrm{s}}\right)\right]\delta_{\mathrm{y}} + \left(1+\alpha\right)\left(\left|\theta_{\mathrm{p}}^{+}\right| + \left|\theta_{\mathrm{p}}^{-}\right|\right)\frac{d'}{2} + \left(1+\alpha\right)\sum_{i=1}^{m}\left[\sum_{j=1}^{N_j}\left(\frac{\theta_i d'}{2l_{\mathrm{n}}}\right)^{0.85}\frac{l_{\mathrm{n}}}{4j}\right] \quad (24)$$

Fig. 21 (a)-(d) compares the experimentally measured axial elongation with the axial elongation obtained from the refined model. The calculated axial elongation using Eq. (19) recommended by Lee & Watanabe are plotted in Fig. 21 as well. These figures indicate that the Lee & Watanabe model significantly underestimates the axial elongation because it does not consider the effect of axial tensile force. The proposed refined model can reasonably trace the axial elongation response of RC walls subjected to reverse cyclic loading and axial tension, expect for specimen HSW4. Specimen HSW4 experienced vertical reinforcement yielding and had large initial axial elongation after application of the high-level of axial tensile force, while such initial axial elongation was not included in the refined model.

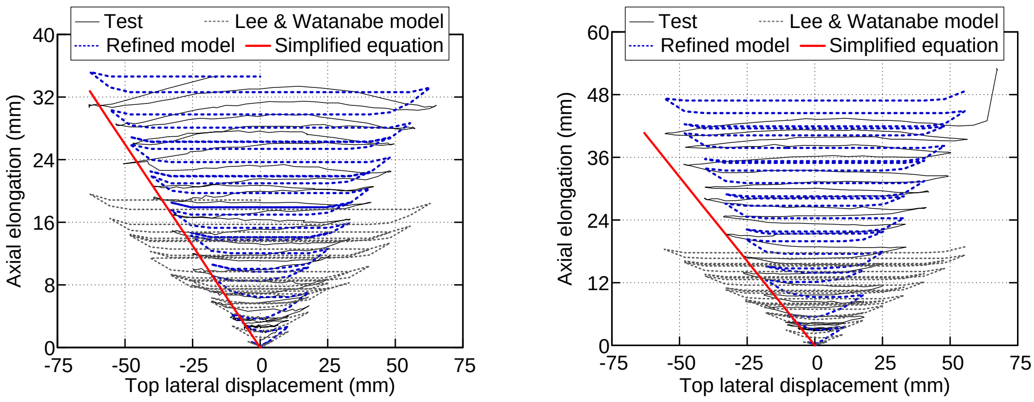

(a) HSW1 (b) HSW2

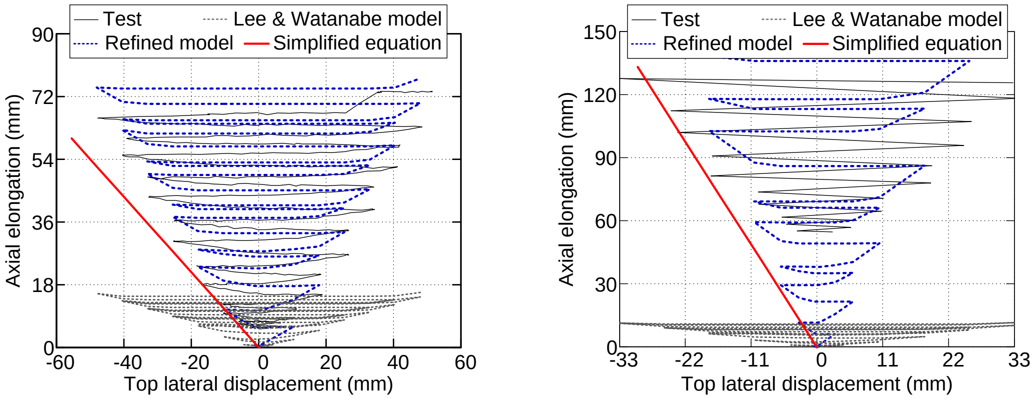

(c) HSW3 (d) HSW4

Fig. 21. Comparision between the measured and calculated axial elongation of test walls.

5.4. Simplified equation for RC wall elongation

While the refined model can accurately predict the axial elongation response of RC walls subjected to reverse cyclic lateral loading and axial tension, the calculation is cumbersome for use in design where only the peak elongations are critical. In order to overcome such complexity, a simple equation is proposed to evaluate the envelope response of axial elongation. Lee & Watanabe [31] found the decreasing rate of the axial elongation in Path 1 and the increasing rate of the axial elongation in path 4 are almost equal. Hence, the axial elongation $\delta_{\text{Path 1}}$ and $\delta_{\text{Path 4}}$ in path 1 and Path 4 are partially eliminated and then the cumulative axial elongation can be obtained in Eq. (25):

$$\delta_{\mathrm{el}} = \delta_{\mathrm{y}} + (1+\alpha)\left(\left|\theta_{\mathrm{p}}^{+}\right| + \left|\theta_{\mathrm{p}}^{-}\right|\right)\frac{d'}{2} \approx (1+\alpha)\theta d' \tag{25}$$

where θ denote the rotations of RC wall plastic hinge. Using the simplified Eq. (25), the envelope curve of axial elongation can be calculated. The comparison between the experimentally observed axial elongation and the simplified envelope curves is also shown in Fig. 21. For specimen HSW1, the simplified equation can accurately predict the axial elongation peaks. However, the simplified equation slightly underestimates the axial elongation of specimens HSW2 and HSW3, which is attributed to the decreasing rate of the axial elongation at the unloading stage might be less than the increasing rate at the reloading stage for the presence of axial tensile force.

In general, the proposed equation can provide reasonable estimation on axial elongation of RC walls under a given plastic rotation and axial tensile force. As the axial elongation of RC walls may result in force redistribution within the structural system, accounting for the wall's axial elongation would improve the seismic design and performance assessment of RC wall structures.

6. Conclusions

This study has presented a series of quasi-static tests to investigate the coupled axial tension-flexure behavior of RC walls, and evaluated the influence of axial tensile forces on the cyclic flexural performance of RC slender walls. The major findings are summarized as follows:

(1) In the coupled tension-flexure tests, RC wall specimens showed two failure modes, defined as flexural-sliding failure (for specimens with normalized concrete tensile stress n_c = 0.33 – 0.98) and flexural failure (for specimen with n_c = 1.73). The flexural-sliding failure had a transition from flexural-dominated deformation to the sliding along the critical crack surface and as such the wall specimens did not fully develop their flexural strength capacity. The wall specimen that failed in a flexural mode did successfully develop its flexural strength capacity.

(2) The effective flexural stiffness of test walls decreased with an increase of axial tension forces. Various design formula of effective flexural stiffness for cracked walls

have been compared using the test data. The ACI 318-14 and ASCE/SEI 41-13 code provisions significantly overestimated the effective flexural stiffness of RC walls subjected to axial tension. Although the equations proposed by Paulay & Priestley and Adebar et al. consider the influence of axial forces, they did not provide an accurate prediction of the effective flexural stiffness of RC walls under axial tension.

(3) Both sectional analysis using XTRACT and design equations per JGJ 3-2010 (China) code provided an accurate estimate of the flexural yield strength of the test walls. For the specimen under high axial tension ($n_c = 1.73$), its hysteretic response was dominated by cyclic behavior of vertical reinforcement, and cyclic hardening of rebar resulted in large post-yield overstrength of the wall.

(4) The axial elongations of RC wall specimens developed during cyclic lateral loading were approximately proportional to the axial tensile force level. A refined model was proposed to estimate the axial elongation response of RC walls including the influence of axial tensile forces. The refined model can accurately trace the measured axial elongation response for the RC test walls subjected to reversed cyclic loading and axial tensile force. Finally, a simplified equation was proposed that can estimate the envelope response of the axial elongation of RC walls. Reasonable calculation of axial elongation of RC walls is useful for improved seismic design and performance assessment of structural wall systems.

Acknowledgements

The authors gratefully acknowledge sponsorship by the National Key R&D Program of China (Grant No. 2017YFC1500602)), National Natural Science Foundation of China

(Grant No. 51678347 and 51811540032), and Beijing Natural Science Foundation (Grant No. JQ18029). The writers wish to express their sincere gratitude to the sponsors.

References

[1] Kato H, Tajiri S. Preliminary reconnaissance report of the Chile earthquake 2010. Building Research Institute, Japan; 2010.

[2] Paulay T, Santhakumar AR. Ductile behavior of coupled shear walls. ASCE J Struct Div 1976; 102(1):93–108.

[3] Aktan AE, Bertero VV. Seismic response of r/c frame-wall structures. J Struct Engng 1984; 110(8):1803–21.

[4] Xu P, Xue Y, Xiao C, Wang C, Sun H, Xu Z, Gu R. Experimental study on seismic performance of high-rise SRC hybrid structures. Build Struct 2005; 35(5):3-8 [in Chinese].

[5] Lehman DE, Turgeon JA, Birely AC, Hart CR, Marley KP, Kuchma DA, Lowes LN. Seismic behavior of a modern concrete coupled wall. J Struct Eng 2013; 139:1371–81.

[6] Wang T, Lai T, Zhao H, Lin H, Wang Y. Tensile-shear mechanical performance test of reinforced concrete shear wall. J Build Struct 2017; 47(2):64-69 [in Chinese].

[7] Ren C, Xiao C, Xu P. Experimental study on tension-shear performance of reinforced concrete shear wall. Chin Civil Eng J 2018; 51(4):20-33 [in Chinese].

[8] Ji X, Cheng X, Xu M. Coupled axial tension-shear behavior of reinforced concrete walls. Eng Struct 2008; 167: 132-42.

[9] ACI 318 Committee. Building Code Requirements for Structural Concrete (ACI

318-14) and Commentary. Farmington Hills (MI): American Concrete Institute; 2014.

[10] CMC. Technical Specification for Concrete Structures of Tall Building (JGJ 3-2010). Beijing: China Ministry of Construction; 2010 [in Chinese].

[11] CMC. Code for Design of Concrete Structures (GB50010-2010). Beijing: China Ministry of Construction; 2010 [in Chinese].

[12] CMC. Chinese Technical Guideline of Peer Review for Seismic Design of Super-Tall Buildings. Beijing: China Ministry of Construction; 2003 [in Chinese].

[13] Ji X, Cheng X, Jia X, Varma AH. Cyclic in-plane shear behavior of double-skin composite walls in high-rise buildings. J Struct Eng 2017; 143(6):04017025.

[14] Ji X, Sun Y, Qian J, Lu X. Seismic behavior and modeling of steel reinforced concrete (SRC) walls. Earthquake Eng Struct Dynam 2015; 44(6):955–72.

[15] Ji X, Leong T, Qian J, Qi W, Yang W. Cyclic shear behavior of composite walls with encased steel braces. Eng Struct 2016; 127:117-128.

[16] Ji X, Jiang F, Qian J. Seismic behavior of steel tube–double steel plate–concrete composite walls: Experimental tests. J Constr Steel Res 2013; 86(6):17–30.

[17] CMC. Specification of Testing Methods for Earthquake Resistant Building. (JGJ 101-2015). Beijing: China Ministry of Construction; 2015. [in Chinese]

[18] Dashti F, Dhakal RP, Pampanin S. Evolution of out-of-plane deformation and subsequent instability in rectangular RC walls under in-plane cyclic loading: Experimental observation. Earthquake Eng Struct Dynam 2018; 47(15):2944–64.

[19] Imbsen and Associates Inc. XTRACT-Cross Section Analysis Program for

Structural Engineers-Step by Step Examples, IMBSEN Software Systems v. 3.0.8, California, 2007.

[20] Massone LM, Wallace JW. Load – deformation responses of slender reinforced concrete walls. ACI Struct J 2004;101(1):103–13.

[21] ASCE. Seismic Rehabilitation of Existing Buildings. ASCE/SEI 41-13. Reston, VA: American Society of Civil Engineers; 2014.

[22] Paulay T, Priestley MJN. Seismic design of reinforced concrete and masonry buildings. John Wiley & Sons, New York; 1992.

[23] Adebar P, Ibrahim AMM, Bryson M. Test of high-rise core wall: effective stiffness for seismic analysis. ACI Structural Journal 2007; 104(5):549–559.

[24] Eurocode 8. Design of Structures for Earthquake Resistance—Part 1: General Rules, Seismic Actions and Rules for Buildings. CEN, Brussels, 1998-1, 2004.

[25] NZS 3101:2006. Concrete Structures Standard (Amendment 3). Wellington, New Zealand: Standards New Zealand; 2017.

[26] Scott BD, Park R, Priestley MJN. Stress-strain behavior of concrete confined by overlapping hoops at low and high strain rates. ACI Struct J 1982; 79(2): 13-27.

[27] Saatcioglu M, Razvi SR. Strength and ductility of confined concrete. J Struct Eng 1992; 118(6):1590–07.

[28] Esmaeily A, Xiao Y. Behavior of reinforced concrete columns under variable axial loads: analysis. ACI Struct J 2005; 102(5):736–44.

[29] Encina E, Lu Y, Henry RS. Axial elongation in ductile reinforced concrete walls. Bull NZ Soc Earthq Eng 2016; 49(4):305-18.

[30] Matthews JG, Mander JB, Bull DK. Prediction of beam elongation in structural concrete members using a rainflow method. NZSEE Annual Conference 2004; Wellington, New Zealand.

[31] Lee JY, Watanabe F. Predicting the longitudinal axial strain in the plastic hinge regions of reinforced concrete beams subjected to reversed cyclic loading. Eng Struct 2003; 25(7):927–39.

[32] Jensen JP. The seismic behaviour of existing hollowcore seating connections pre and post retrofit. M.S. Christchurch: University of Canterbury Civil Engineering; 2007.

[33] Moehle J. Seismic design of reinforced concrete buildings. New York: McGraw-Hill Education; 2014.